Efficient Photocatalytic CO$_2$ Reduction with MIL-100(Fe)-CsPbBr$_3$ Composites

Ruolin Cheng [1], **Elke Debroye [1]**, **Johan Hofkens [1],*** **and Maarten B. J. Roeffaers [2],***

[1] Department of Chemistry, Faculty of Sciences, KU Leuven, Celestijnenlaan 200F, 3001 Leuven, Belgium; ruolin.cheng@kuleuven.be (R.C.); elke.debroye@kuleuven.be (E.D.)

[2] Center for Membrane Separations, Adsorption, Catalysis and Spectroscopy for Sustainable Solutions (cMACS), KU Leuven, Celestijnenlaan 200F, 3001 Leuven, Belgium

* Correspondence: johan.hofkens@kuleuven.be (J.H.); maarten.roeffaers@kuleuven.be (M.B.J.R.); Tel.: +32-16-327804 (J.H.); +32-16-327449 (M.B.J.R.)

check for updates

Abstract: Bromide-based metal halide perovskites (MHPs) are promising photocatalysts with strong blue-green light absorption. Composite photocatalysts of MHPs with MIL-100(Fe), as a powerful photocatalyst itself, have been investigated to extend the responsiveness towards red light. The composites, with a high specific surface area, display an enhanced solar light response, and the improved charge carrier separation in the heterojunctions is employed to maximize the photocatalytic performance. Optimization of the relative composition, with the formation of a dual-phase CsPbBr$_3$ to CsPb$_2$Br$_5$ perovskite composite, shows an excellent photocatalytic performance with 20.4 µmol CO produced per gram of photocatalyst during one hour of visible light irradiation.

Keywords: metal halide perovskites; metal-organic framework; photocatalysis

1. Introduction

The capture of CO$_2$ and further conversion of this greenhouse gas into chemical fuels (CO, CH$_4$, CH$_3$OH, etc.) has been a hot topic during the past decades [1]. The reduction of CO$_2$ is complicated by its inherent chemical stability [2,3]. Despite this issue, photocatalytic CO$_2$ reduction is still seen as one of the promising ways to sustainably produce chemicals [4]. To date, a wide variety of photocatalysts such as TiO$_2$, ZnO, CdS, perovskite oxides and their composites, and metal (complex) functionalized derivatives, have been tested. But the obtained performances under solar irradiation are still limited, mainly due to the low efficiency of using visible light.

Over the last decades, metal-organic frameworks (MOFs) have been one of the fastest developing materials, exhibiting unique properties such as structural flexibility, large specific surface area, tunable but uniform cavities, and easy ligand functionalization [5,6]. MOF-5 was the first MOF reported to have photocatalytic activity in UV-induced phenol photodegradation [7]. Fu et al. successfully employed an amine-functionalized Ti-based MOF, NH$_2$-MIL-125(Ti), in CO$_2$ photoreduction [8]. Ever since, MOFs are not only used as matrix for other semiconductors or noble metals but are also seen as promising photocatalysts on their own [9–11].

Recently, all-inorganic CsPbBr$_3$ perovskites have emerged as promising photocatalysts in various applications ranging from dye degradation [12] to selective organic reactions [13] and renewable fuel generation from CO$_2$ and water [14]. These materials combine the excellent optoelectronic properties of organic-inorganic hybrid perovskites, such as a bandgap largely overlapping with the visible part of the electromagnetic spectrum, a high absorption coefficient, and long-range charge transport, with good temperature stability [15,16]. However, the performances of MHPs are limited by their poor structural stability in a humid atmosphere. Heterojunction formation with materials such as graphene oxide,

MOFs, TiO_2, C_3N_4, etc., has been explored to further improve charge carrier separation and protect the MHPs from a polar environment [17–21]. The use of MOFs in combination with MHPs is motivated by the composites improved stability as compared to the parent MHP material in photocatalytic reactions in the presence of water.

Herein, we report the excellent performance of $CsPbBr_3$/MIL-100(Fe) composites for the photocatalytic reduction of CO_2. Among the reported MOF photocatalysts, Fe-based MIL-100 was chosen due to its low cost, high chemical and water stability, and the intense and complementary visible light absorption to the far red [22,23]. We reasoned that the $CsPbBr_3$/MIL-100(Fe) composite should show an extended and improved absorption and hence has the potential to be an efficient photocatalyst. The composite material was generated through the in situ synthesis of MIL-100(Fe) on perovskite particles, which tends to improve the stability of the composite and offers more efficient electron transfer [24]. MIL-100(Fe) introduction endows the composite with a high specific surface area and enhanced visible light response.
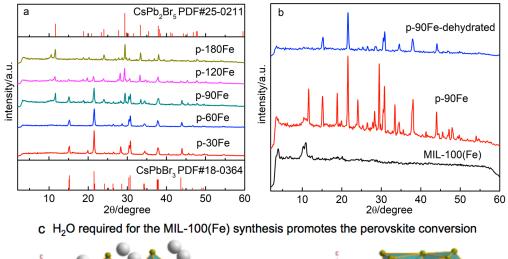
2. Results

Pure $CsPbBr_3$ was synthesized using an anti-solvent method and MIL-100(Fe) was synthesized by a modified non-hydrothermal method (see Section 3). The composite photocatalysts were obtained by an in situ growth method and were named after the amount of MIL-100(Fe) precursor ($Fe(NO_3)_3 \cdot 9H_2O$) added (see Section 3).

In the first step, X-ray diffraction (XRD) was used to investigate the crystallinity of the pure and composite materials (Figure 1a). The XRD patterns clearly show the orthorhombic $CsPbBr_3$ structure and in the composite materials, additional diffraction peaks at 3.4° and 11° from MIL-100(Fe) appear (Figure 1b) [25,26]. With an increasing amount of MIL-100(Fe) loaded in the composites, we observe a gradual transformation of $CsPbBr_3$ (PDF#18-0364) to $CsPb_2Br_5$ (PDF#25-0211). Figure 1c illustrates the perovskites' crystallographic structure transformation. This phase transformation could be ascribed to the excessive H_2O in the Fe precursor, which partially converts the $CsPbBr_3$. To evaluate the necessity of H_2O during the in-situ growth of the MOF, the Fe precursor was dried ahead of the synthesis. With this dried $Fe(NO_3)_3$ precursor, the desired MIL-100(Fe) could not be generated (Figure 1b), indicating the critical role of water during the MIL-100(Fe) formation, in line with literature reports [10].

The Fourier-transform infrared (FTIR) spectra of all composites exhibit typical MIL-100(Fe) bands (Figure 2a) [27]. The bands at 1625 and 1380 cm^{-1} are related to the stretching vibrations of carboxyl groups [28], the band at 1446 cm^{-1} can be ascribed to the O–H stretching vibration, while the ones corresponding to the bending vibration of C–H (at 759 cm^{-1}) and C=C (at 711 cm^{-1}) originate from the benzene ring. As expected, the peak intensities of the Fe-O stretching vibration (at 491 cm^{-1}) and free C=O stretching vibration from unreacted H_3BTC (at 1716 cm^{-1}) enhanced with increasing the amount of MIL-100(Fe) loaded in the composites [29]. Further, a broad peak at 3000–3500 cm^{-1} indicates the presence of a significant amount of adsorbed H_2O in the composites.

Thermogravimetric analysis (TGA) was performed in O_2 to quantify the MIL-100(Fe) amount in the composites based on the oxidation of the organic linker (Figure 2b). MIL-100(Fe) exhibits a clear two-step weight loss: (1) below 200 °C, the weight loss is associated with the removal of adsorbed H_2O, and H_2O coordinated to the iron trimers, (2) around 300 °C, H_3BTC decomposes [30]. This two-step weight loss was identified in all the composites. $CsPbBr_3$ shows a good thermal stability to about 500 °C. Hence, the weight loss due to H_3BTC decomposition was used to determine the relative amount of MIL-100(Fe) in the composites. As listed in Table 1, the MIL-100(Fe) content in the composites varies from 9 wt% in p-30Fe to 53 wt% in p-180Fe.
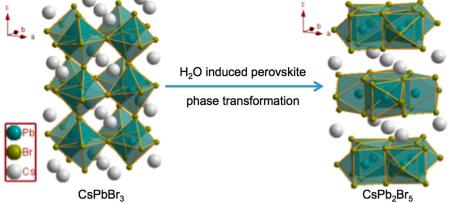
Figure 1. (**a**,**b**) XRD patterns of the as-prepared photocatalysts, and (**c**) visualization of the perovskites' crystallographic structure transformation.
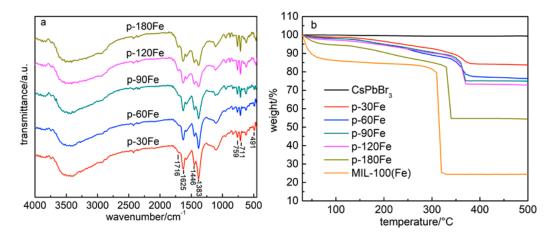

Figure 2. (**a**) FTIR spectra, and (**b**) TGA thermograms of the as-prepared photocatalysts.

Table 1. Weight ratio of MIL-100(Fe) in the composites.

Sample	p-30Fe	p-60Fe	p-90Fe	p-120Fe	p-180Fe
MIL-100(Fe) content/wt%	9	14	18	27	53

The surface chemical composition and chemical states of the as-synthesized composites were further revealed by X-ray photoelectron spectroscopy (XPS). The XPS spectrum (Figure 3a) of p-90Fe shows distinct peaks from both of MIL-100(Fe) and $CsPbBr_3$. Relevant high-resolution spectra of p-90Fe (Figure S1) display peaks of Cs 3d, Pb 4f, and Br 3d in the range of 720–745, 134–148, and 64–74 eV, respectively, which are well-matched with those of $CsPbBr_3$ [31,32]. Two dominant peaks of Fe (Figure 3b) at 724.6 and 711.7 eV are attributed to Fe $2p_{1/2}$ and Fe $2p_{3/2}$, respectively. Additional satellite peak appearing at 717.2 eV corresponds to Fe^{3+} in MIL-100(Fe) [33].
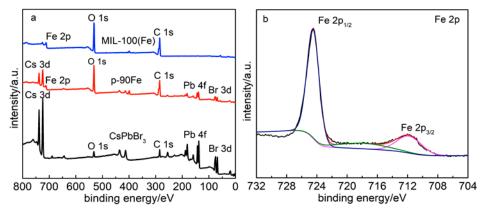

Figure 3. XPS spectra of p-90Fe: (**a**) survey and (**b**) Fe 2p.

The response of MIL-100(Fe) in the visible light region arises from the direct excitation of the Fe–O clusters. As shown in the absorption spectra in Figure 4a (as obtained by UV-vis diffuse reflectance, see Section 3), p-30Fe, p-60Fe, and p-90Fe basically maintain the pattern of $CsPbBr_3$. p-120Fe and p-180Fe exhibit a pattern similar to MIL-100(Fe), due to the larger amount of MIL-100(Fe) included. The addition of MIL-100(Fe) enhances the composites' optical response in the visible light region, especially above 550 nm. The absorption edges around 550 nm gradually blue shift, corresponding to the increased bandgaps (E_g) (calculated by the Tauc plots, Figure 4b) of the composites consisting of more MIL-100(Fe) (Table 2). This blue-shift arises from the phase transformation from $CsPbBr_3$ (E_g = 2.3 eV) to $CsPb_2Br_5$ (E_g = 3.0 eV) and the more dominant role of MIL-100(Fe) in the composite photocatalysts upon increasing the Fe content.
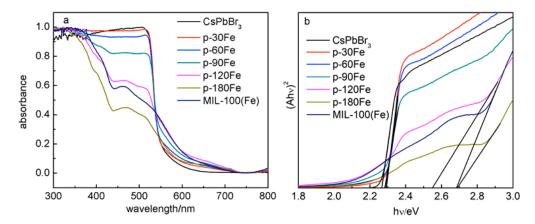

Figure 4. (**a**) UV-vis absorption spectra of parent compounds and composites, and (**b**) Tauc plots of MIL-100(Fe) and the composites. The band gap energies of the photocatalysts, listed in Table 2, were estimated following Kubelka-Munk transformation. Each bandgap is determined by the intersection point of the corresponding tangent line and horizontal axis.

Table 2. Bandgap data of the prepared samples.

Sample	MIL-100(Fe)	CsPbBr$_3$	p-30Fe	p-60Fe	p-90Fe	p-120Fe	p-180Fe
E$_g$/eV	2.68	2.27	2.29	2.29	2.30	2.55	2.69

Figure 5 and Figure S2 show the steady-state photoluminescence (PL) spectra of the photocatalysts at an excitation wavelength of 380 nm. As shown in Figure S2, CsPbBr$_3$ has significantly higher peak intensity than the composites. The broad emission peak from 400 to 450 nm can be attributed to the 1,3,5-benzene tricarboxylic acid linkers in the MIL-100(Fe) structure [34]. The PL emission spectra of p-30Fe, p-60Fe and p-90Fe show a gradual blue shift and weakening intensity of the peak at around 530 nm. Different from 3D CsPbBr$_3$, Cs$^+$ ions separate the layers of 2D CsPb$_2$Br$_5$, and the excitons are slowed down by the layered structure [35]. Thus, with more CsPb$_2$Br$_5$ formed, the PL peaks of p-120Fe and p-180Fe get more blue shifted [36,37]. p-90Fe possesses the lowest PL intensity among all as-synthesized CsPbBr$_3$/MIL-100(Fe) samples.
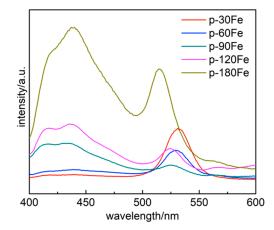

Figure 5. Steady-state PL spectra at an excitation wavelength of 380 nm of the composites. PL spectra of the parent compounds in Supplementary Materials.

As shown in Figure S3a, the pure CsPbBr$_3$ sample displays nanoparticles with a uniform cubic shape. MIL-100(Fe) synthesized in HF-free conditions crystallizes into small nanoparticles with no clearly visible shape compared to the classic octahedral shapes (Figure S3b); this is in line with previous reports [38]. In the composite materials, e.g., p-90Fe, the cubic CsPbBr$_3$ morphology is lost and only agglomerated particles are observed (Figure S3c). Selected location elemental analysis by energy-dispersive X-ray spectroscopy (EDS) confirms the co-existence of both CsPbBr$_3$ and MIL-100(Fe) (Figure S3d).

The components' dispersion and interaction were studied by confocal laser scanning fluorescence measurements on p-90Fe, using a 375 nm laser. Figure 6d showed the wide field image of p-90Fe. Based on the PL spectra mentioned above, two emission channels at 430–470 nm and 505–540 nm were chosen to visualize the MIL-100(Fe) (red colored) (Figure 6a) and CsPbBr$_3$ (green colored) (Figure 6b) distribution, respectively. Both channels were acquired with the same excitation power. As CsPbBr$_3$ has a significantly stronger signal than MIL-100(Fe) upon excitation (Figure S2), Figure 6a was adjusted to be 25% brighter than Figure 6b.

As shown in Figure 6c, yellow shaded areas appear where both signals overlap. Based on particle count, ca. 80% particles were yellowish-green. These uniformly dispersed yellow shades reflect the close contact between MOF and MHP parts in the composite.

The complementary light absorption by CsPbBr$_3$ and MIL-100(Fe) should result in an efficient photocatalytic activity under simulated solar irradiation. Here, CO$_2$ photoreduction under visible light irradiation was chosen to test the photoactivity of the different catalysts. The reaction was performed under 1 bar hydrated CO$_2$ atmosphere, at ambient temperature. CO was found as the

only photoreduction product generated from CO_2, and no other carbonaceous products was detected. A series of control experiments were also conducted. No appreciable amounts of CO or other hydrocarbons were detected in the absence of light irradiation, or photocatalyst, or CO_2 (under wet He atmosphere).
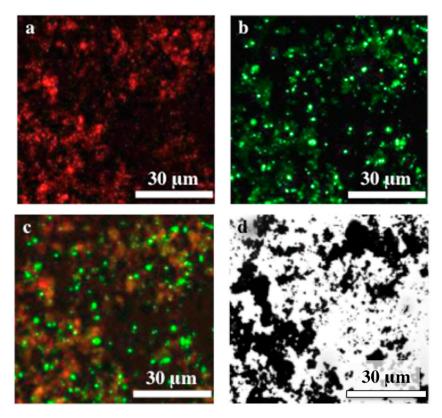

Figure 6. Confocal fluorescence scanning images of (**a**) 430–470 nm emission and (**b**) 505–540 nm emission, (**c**) overlapped image of (**a**,**b**), and (**d**) wide field image, using a 375 nm laser excitation of p-90Fe.

Figure 7a shows the time-dependent CO production on the as-synthesized samples during a 4 h experiment. The CO production rate over pure $CsPbBr_3$ and MIL-100(Fe) are similar, about 4.5 μmol g^{-1} h^{-1}. The composite materials show significantly higher activity, and p-90Fe exhibits a maximum CO production of 20.4 μmol g^{-1} h^{-1}, which is about 4.5 times higher than the pure constituents. Upon increasing the load of MIL-100(Fe), lower photocatalytic activity is obtained. The decrease in photocatalytic activity may be caused by an increasing amount of $CsPb_2Br_5$ in the composites, which is not active upon visible light irradiation. The critical role of H_2O was revealed by a test reaction on p-90Fe in high purity CO_2 gas without H_2O. The CO yield over p-90Fe dropped from 20.4 to 5.3 μmol g^{-1} h^{-1}. The composites' stability was evaluated by four consecutive runs (4 h each, in total 16 h) on p-90Fe. As shown in Figure 7b, the composite exhibits no significant deactivation, and its crystal structure is well maintained after the 16 h photocatalytic reaction (Figure S4).

Two reference samples, p-post and p-mix, with the same amount of MIL-100(Fe) loaded as p-90Fe, were constructed. p-post was synthesized by the anti-solvent deposition of $CsPbBr_3$ onto MIL-100(Fe) [39]. p-mix was prepared through ultrasonically mixing the $CsPbBr_3$ and MIL-100(Fe) powders. Under visible light irradiation, the CO production rates over p-post and p-mix are only 8.7 μmol g^{-1} h^{-1} and 6.8 μmol g^{-1} h^{-1}, nearly one-third of that obtained via the newly introduced in situ growth route. A summary of the reported photocatalytic CO_2 reduction performance on perovskite-based and traditional photocatalysts under various illumination conditions is listed in Table S1.
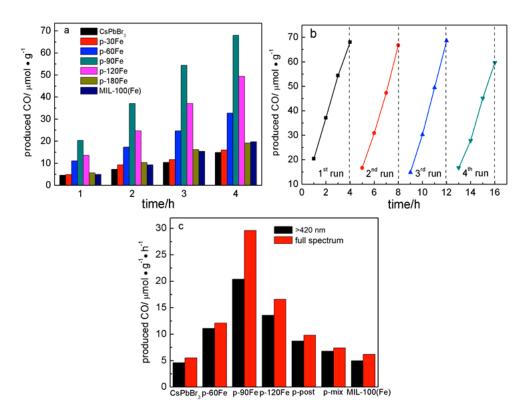
Figure 7. (**a**) Time-dependent CO generation over the synthesized MIL-100(Fe), CsPbBr$_3$, and composites, (**b**) Stability test on p-90Fe for four consecutive runs (4 h each, in total 16 h), and (**c**) CO generation over the photocatalysts under different illumination conditions.

It is observed that CsPbBr$_3$ gradually transforms to CsPb$_2$Br$_5$ in the composites, and CsPb$_2$Br$_5$ is a large bandgap material without visible light response. Therefore, full-spectrum (300–800 nm) measurements were performed on the selected samples to investigate the photocatalytic contribution of CsPb$_2$Br$_5$ in the composites. As shown in Figure 7c, only slight improvements in CO generation were found on CsPbBr$_3$, p-post, and p-mix, compared to that under visible light irradiation (420–800 nm). The CO generation significantly enhanced from 20.4 to 29.6 μmol g^{-1} h^{-1} on p-90Fe and from 13.6 to 16.6 μmol g^{-1} h^{-1} on p-120Fe. Hence, CsPb$_2$Br$_5$, used to be seen as the undesirable byproduct of CsPbBr$_3$, can contribute to the composites' photoactivity.

It is acknowledged that the photocatalysts' performance can be influenced by the specific surface area. First, gas sorption measurements were performed (Figure S5a). N$_2$ physisorption revealed a negligible surface area for the pure CsPbBr$_3$ microcrystals. The composite materials show a tremendously increased specific surface area between 130 and 400 m^2/g (Table 3); the specific surface area increases with the amount of MIL-100(Fe). This surface area enhancement favors the exposure of active sites and the adsorption of CO$_2$ molecules. For the composites, a type IV isotherm is observed related to the existence of a mesoporous structure. Further, Figure S5b shows the CO$_2$ adsorption isotherms of the as-obtained samples. The CO$_2$ uptakes in the composites are 15 to 30 times higher than that in pure CsPbBr$_3$, which benefits the photocatalytic efficiency. Figure S6 shows the N$_2$ physisorption isotherms and related pore size distribution of p-90Fe before and after the reaction. After the reaction, the surface area reduced from 201 m^2/g to 155 m^2/g, the average pore size decreased from 4.5 nm to 3.7 nm, and the pore volume dropped from 0.21 cm^3/g to 0.11 cm^3/g. As can be seen in Figure S6b, p-90Fe has dominant peaks at 1.2 and 2.0 nm, which is the typical pore size distribution of MIL-100(Fe) [40]. After the reaction, the portion of the mesopores around 10 nm decreased, which may be due to the influence of H$_2$O on the particle size and shape during the reaction.

Table 3. The specific surface area of the prepared composites.

Sample	p-60Fe	p-90Fe	p-120Fe	p-180Fe
S_{BET}/m^2 g^{-1}	130	201	277	390

As shown in Figure 8, the PL decay plots of $CsPbBr_3$ and composite p-90Fe are fitted with a biexponential decay function. The short and long PL lifetimes can be assigned to two different physical origins. The short (τ_1) and long (τ_2) lifetimes are related to the trap-assisted and exciton recombination, respectively [13]. The average lifetime (τ) of $CsPbBr_3$ exhibits an obvious decrease from 4.4 to 1.6 ns after adding MOF, resulting from the suppressed exciton recombination. MIL-100(Fe) here functions as a quencher of $CsPbBr_3$, endowing the composite with a more effective electron extraction [41].
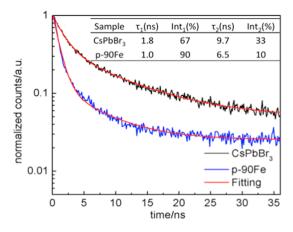

Sample	τ_1(ns)	Int_1(%)	τ_2(ns)	Int_2(%)
$CsPbBr_3$	1.8	67	9.7	33
p-90Fe	1.0	90	6.5	10

Figure 8. Time-resolved PL spectra of pure $CsPbBr_3$ and p-90Fe fitted with a biexponential decay kinetic, including the corresponding fitting parameters.

The photocatalytic activity of MIL-100(Fe) mainly originates from the direct excitation of the Fe_3–μ_3–oxo clusters inside the structure. Under light irradiation, Fe–O clusters in MIL-100(Fe) can be excited, transferring an electron from the O^{2-} to Fe^{3+} for the formation of Fe^{2+}, which is responsible for CO_2 reduction over pure MIL-100(Fe) [22,42]. The combination of the bandgap data with valence band measurements (Figure S7 and Table 2) allow to determine the VB and CB edge potentials of $CsPbBr_3$ to be 0.82 and −1.45 eV, respectively. The VB and CB edge potentials of MIL-100(Fe) are calculated to be 1.75 and −0.93 eV, respectively. Therefore, a typical type II heterojunction was formed by the perfect band structure matching of $CsPbBr_3$ and MIL-100(Fe) [42].

A possible mechanism for the visible-light driven photocatalytic CO_2 reduction over the composite is proposed, as shown in Figure 9. Photo-induced electron and hole pairs are generated on $CsPbBr_3$ and MIL-100(Fe) and tend to transfer. The electrons in the conduction band of $CsPbBr_3$ will transfer to that of MIL-100(Fe), where CO_2 would be reduced to CO. The holes on the valence band of MIL-100(Fe) would migrate to that of $CsPbBr_3$, where H_2O will be trapped to generate O_2.
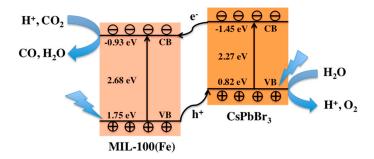

Figure 9. Schematics of the CO_2 photoreduction process on $CsPbBr_3$/MIL-100(Fe) under visible light irradiation.

With H_2O involved in the synthesis, $CsPbBr_3$ gradually converts to $CsPb_2Br_5$, which has no visible light response. Revealed by the XRD and UV-vis absorption spectra, p-90Fe has the highest amount of MIL-100(Fe) in the composite while maximally retaining $CsPbBr_3$. MIL-100(Fe) greatly increases the surface area and enhances the visible light absorption ability of $CsPbBr_3$. Upon visible light irradiation, the separation and transfer of the photogenerated charge carriers is promoted in the composites, resulting in enhanced photocatalytic performance. Further increasing the amount of MIL-100(Fe) increases the specific surface area and CO_2 uptake, but at the expense of $CsPbBr_3$.

3. Materials and Methods

3.1. Catalyst Synthesis

3.1.1. Synthesis of CsPbBr3

$CsPbBr_3$ was synthesized by the anti-solvent method. 2.5 mmol cesium bromide (CsBr, 99.9%, Alfa Aesar, Kandel, Germany) and 2 mmol lead (II) bromide ($PbBr_2$, 99.999%, Alfa Aesar, Kandel, Germany) were dissolved in 15 mL dimethyl sulphoxide (DMSO, ≥99.9%, ACS reagent, Sigma-Aldrich, Overijse, Belgium) and stirred for 12 h. The solution was quickly added into 150 mL toluene under stirring. The obtained product was collected by centrifugation, washed with toluene, and dried in a vacuum oven at 80 °C.

3.1.2. Synthesis of Pure MIL-100(Fe)

In a typical procedure, 2.02 g iron (III) nitrate nonahydrate ($Fe(NO_3)_3 \cdot 9H_2O$)(99%, ACROS Organics, Geel, Belgium), and 0.7 g 1,3,5-benzenetricarboxylic acid (H_3BTC, 95%, Sigma-Aldrich, Overijse, Belgium) were added to 5 mL H_2O and stirred for 30 min at RT. This mixture was then heated to 95 °C and maintained at this temperature for 12 h. After cooling down the mixture, the obtained orange solid product was collected by centrifugation, washed with distilled water, and dried at 80 °C.

3.1.3. Synthesis of the CsPbBr3/MIL-100(Fe) Composites

The $CsPbBr_3$/MIL-100(Fe) composites were obtained by in situ growth. The Fe precursor solution for MIL-100(Fe) was made first, by adding 30, 60, 90, 120, and 180 mg $Fe(NO_3)_3 \cdot 9H_2O$ into 3 mL 1-propanol (99.5%, ACS agent, Fisher Chemical, Merelbeke, Belgium). Next, 0.1 g $CsPbBr_3$ was added to this Fe precursor solution and the mixture was stirred for 12 h at RT. The H_3BTC powder was then added with a 3:1 molar ratio of H_3BTC to $Fe(NO_3)_3 \cdot 9H_2O$. The mixture was heated to 95 °C and kept at this temperature for 12 h. The resulting orange solid product was collected by centrifugation, washed by toluene, and dried at 100 °C in a vacuum oven. The obtained samples were named as p-xFe (x = the weight of $Fe(NO_3)_3 \cdot 9H_2O$ added).

For comparison, $CsPbBr_3$ was loaded onto MIL-100(Fe) by anti-solvent deposition [39]. This sample is named as p-post. Furthermore, a physical mixture of the pure $CsPbBr_3$ and MIL-100(Fe) was prepared by ultrasonically mixing the powders, named as p-mix. The weight ratios of MIL-100(Fe) in both p-post and p-mix are 18 wt%. Finally, 90 mg $Fe(NO_3)_3 \cdot 9H_2O$ was dehydrated in a vacuum oven at 80 °C for 4 h before the composite synthesis, and the obtained sample was named as p-90Fe-dehydrated.

3.2. Characterization

X-ray diffraction (XRD) patterns were recorded on a Malvern PANalytical Empyrean system (Malvern PANalytical, Hoeilaart, Belgium). Scanning electron microscopy (SEM) images and the corresponding energy dispersive X-ray spectroscopy (EDS) data were taken with a FEI-Q FEG250 system (Thermo Fisher Scientific, Zaventem, Belgium). X-ray photoelectron spectroscopy (XPS) data were recorded on an ESCALAB 250 spectrometer (Thermo Fisher Scientific, Beijing, China) with a monochromatized Al Ka X-ray as the excitation source, and the binding energies were calibrated by the C1s peak at 284.8 eV. Gas sorption measurements were performed on a 3Flex Surface Analyzer

(Micromeritics, Unterschleissheim, Germany) where nitrogen (N_2) adsorption-desorption isotherms were acquired at −196 °C and CO_2 adsorption isotherm were acquired at 0 °C. Before the measurement, all the samples were degassed at 150 °C for 8 h under flowing N_2. Thermogravimetric analysis (TGA) was performed from room temperature to 800 °C at a heating rate of 10 °C min^{-1} in O_2 on a TA-TGA Q500 (TA Instruments, Antwerp, Belgium). Fourier transformed infrared (FTIR) spectra were collected using a Bruker FTIR spectrophotometer (Bruker, Kontich, Belgium). UV-Vis diffuse reflectance spectra were recorded with a Lambda-950 UV-Vis spectrometer (PerkinElmer, Mechelen, Belgium). The steady-state photoluminescence (PL) spectra were acquired on an Edinburgh FLS980 instrument (Edinburgh Instruments Ltd, Livingston, UK). The samples were prepared by filling a thin quartz cuvette (Macro cell 110-QS, 1 mm light path, Hellma, Kruibeke, Belgium) with the same volume of powders. Time-resolved PL spectra were acquired by a home-built confocal FLIM microscope, equipped with a single-photon counting device (Picoquant, Berlin, Belgium) Powders of $CsPbBr_3$ and p-90Fe were dispersed in toluene and sonicated for 15 min. The suspension was then dropped onto a 20 × 20 mm cover slide and dried in the vacuum oven at 80 °C overnight. The excitation source was a 5 MHz pulsed 485 nm laser diode, and the emission was filtered by a 530 ± 25 nm band pass filter. Confocal fluorescence images were acquired on a Fluoview FV1000 confocal microscope (Olympus, Tokyo, Japan). An Olympus 20 × 0.75 NA air immersion objective lens was used. A 375 nm laser was used as the excitation source, and the detectors for fluorescence emission were set at 430–470 and 505–540 nm. The image size was 1024 × 768 pixels with a pixel dwell time of 4 μs.

3.3. Photocatalytic CO_2 Reduction Measurement

The photocatalytic reduction of CO_2 was performed in a homemade Pyrex reactor (volume: 150 mL). Visible light was generated by a 300 W Xe lamp with a 420 cut-off filter (Newport, Darmstadt, Germany) and positioned 5 cm away from the photocatalytic reactor. In a typical sample preparation, 20 mg photocatalyst was uniformly dispersed on a flat glass plate with an area of 4 cm^2. The as-prepared sample plate was left in the vacuum oven at 80 °C overnight to remove the residual solvent. Before the reaction, helium flowed through the reactor for about 20 min to eliminate the air inside. Then, a mixture of CO_2 and water vapor, generated by passing high purity CO_2 (99.99%) gas through a water bubbler, flowed through the reactor for another 40 min in the dark. Afterwards, the reactor was closed off and light irradiation was started. The gas sample was evaluated every 1 h by gas chromatography (GC-2014, Shimadzu, Tokyo, Japan) equipped with a ShinCarbon packed column with a flame ionization detector (FID) and a thermal conductivity detector (TCD). The carrier gas used in the GC-2014 was high purity helium. After the 16 h stability test, the sample was collected and treated at 80 °C in the vacuum oven overnight.

4. Conclusions

In summary, we have reported the in situ synthesis of $CsPbBr_3$/MIL-100(Fe) for CO_2 photoreduction under visible light irradiation. Compared to anti-solvent deposition and physical mixing methods, the composites obtained by this new route show a significantly improved CO_2 photoreduction activity. H_2O is necessary for the in situ growth of the MOF structure, but excessive H_2O initiates the transformation of $CsPbBr_3$ to $CsPb_2Br_5$. Through optimization of the composite material composition, the highest CO production rate is 20.4 μmol g^{-1} h^{-1}, which is about 4.5 times that of the parent materials. The composite showed good stability in a 16 h photocatalytic reaction, where H_2O is involved as the reactant. The introduction of MIL-100(Fe) endowed the composites with a largely increased surface area and enhanced light-harvesting capability in the visible light region. The perfect band matching between $CsPbBr_3$ and MIL-100(Fe) attributes to better electron-hole separation and transfer. The findings here could serve as a steppingstone for further developing MHP photocatalysts, involving MOF-based heterojunctions.

References

1. Sun, Z.X.; Wang, H.Q.; Wu, Z.B.A.; Wang, L.Z. g-C_3N_4 based composite photocatalysts for photocatalytic CO_2 reduction. *Catal. Today* **2018**, *300*, 160–172. [CrossRef]

2. Indrakanti, V.P.; Kubicki, J.D.; Schobert, H.H. Photoinduced activation of CO_2 on Ti-based heterogeneous catalysts: Current state, chemical physics-based insights and outlook. *Energy Environ. Sci.* **2009**, *2*, 745–758. [CrossRef]

3. Tran, P.D.; Wong, L.H.; Barber, J.; Loo, J.S.C. Recent advances in hybrid photocatalysts for solar fuel production. *Energy Environ. Sci.* **2012**, *5*, 5902–5918. [CrossRef]

4. Habisreutinger, S.N.; Schmidt-Mende, L.; Stolarczyk, J.K. Photocatalytic reduction of CO_2 on TiO_2 and other semiconductors. *Angew. Chem. Int. Ed.* **2013**, *52*, 7372–7408. [CrossRef] [PubMed]

5. Zhao, M.T.; Huang, Y.; Peng, Y.W.; Huang, Z.Q.; Ma, Q.L.; Zhang, H. Two-Dimensional metal-organic framework nanosheets: Synthesis and applications. *Chem. Soc. Rev.* **2018**, *47*, 6267–6295. [CrossRef] [PubMed]

6. Tu, W.G.; Xu, Y.; Yin, S.M.; Xu, R. Rational design of catalytic centers in crystalline frameworks. *Adv. Mater.* **2018**, *30*, 1707582–1707610. [CrossRef]

7. Alvaro, M.; Carbonell, E.; Ferrer, B.; Xamena, F.X.L.I.; Garcia, H. Semiconductor behavior of a metal-organic framework (MOF). *Chem. Eur. J.* **2007**, *13*, 5106–5112. [CrossRef]

8. Fu, Y.H.; Sun, D.R.; Chen, Y.J.; Huang, R.K.; Ding, Z.X.; Fu, X.Z.; Li, Z.H. An amine-functionalized titanium metal-organic framework photocatalyst with visible-light-induced activity for CO_2 reduction. *Angew. Chem. Int. Ed.* **2012**, *51*, 3364–3367. [CrossRef]

9. Liang, Z.B.; Qu, C.; Xia, D.G.; Zou, R.Q.; Xu, Q. Atomically dispersed metal sites in MOF-based materials for electrocatalytic and photocatalytic energy conversion. *Angew. Chem. Int. Ed.* **2018**, *57*, 9604–9633. [CrossRef]

10. Qiu, J.H.; Zhang, X.G.; Feng, Y.; Zhang, X.F.; Wang, H.T.; Yao, J.F. Modified metal-organic frameworks as photocatalysts. *Appl. Catal. B* **2018**, *231*, 317–342. [CrossRef]

11. Yang, Z.W.; Xu, X.Q.; Liang, X.X.; Lei, C.; Wei, Y.L.; He, P.Q.; Lv, B.L.; Ma, H.C.; Lei, Z.Q. MIL-53(Fe)-graphene nanocomposites: Efficient visible-light photocatalysts for the selective oxidation of alcohols. *Appl. Catal. B* **2016**, *198*, 112–123. [CrossRef]

12. Zhao, Y.; Wang, Y.; Liang, X.; Shi, H.; Wang, C.; Fan, J.; Hu, X.; Liu, E. Enhanced photocatalytic activity of Ag-$CsPbBr_3$/CN composite for broad spectrum photocatalytic degradation of cephalosporin antibiotics 7-ACA. *Appl. Catal. B* **2019**, *247*, 57–69. [CrossRef]

13. Huang, H.W.; Yuan, H.F.; Janssen, K.P.F.; Solis-Fernandez, G.; Wang, Y.; Tan, C.Y.X.; Jonckheere, D.; Debroye, E.; Long, J.L.; Hendrix, J.; et al. Efficient and selective photocatalytic oxidation of benzylic alcohols with hybrid organic-inorganic perovskite materials. *ACS Energy Lett.* **2018**, *3*, 755–759. [CrossRef]

14. Huang, H.W.; Pradhan, B.; Hofkens, J.; Roeffaers, M.B.J.; Steele, J.A. Solar-Driven metal halide perovskite photocatalysis: Design, stability, and performance. *ACS Energy Lett.* **2020**, *5*, 1107–1123. [CrossRef]

15. Kang, B.; Biswas, K. Exploring polaronic, excitonic structures and luminescence in Cs$_4$PbBr$_6$/CsPbBr$_3$. *J. Phys. Chem. Lett.* **2018**, *9*, 830–836. [CrossRef]

16. Dana, J.; Maity, P.; Jana, B.; Maiti, S.; Ghosh, H.N. Concurrent ultrafast electron- and hole-transfer dynamics in CsPbBr$_3$ perovskite and quantum Dots. *ACS Omega* **2018**, *3*, 2706–2714. [CrossRef] [PubMed]

17. Cheng, R.L.; Jin, H.D.; Roeffaers, M.B.J.; Hofkens, J. Incorporation of cesium lead halide perovskites into g-C$_3$N$_4$ for photocatalytic CO$_2$ Reduction. *ACS Omega* **2020**, *5*, 24495–24503. [CrossRef] [PubMed]

18. Xu, Y.F.; Yang, M.Z.; Chen, B.X.; Wang, X.D.; Chen, H.Y.; Kuang, D.B.; Su, C.Y. A CsPbBr$_3$ perovskite quantum dot/graphene oxide composite for photocatalytic CO$_2$ reduction. *J. Am. Chem. Soc.* **2017**, *139*, 5660–5663. [CrossRef]

19. Kong, Z.C.; Liao, J.F.; Dong, Y.J.; Xu, Y.F.; Chen, H.Y.; Kuang, D.B.; Su, C.Y. Core@shell CsPbBr$_3$@zeolitic imidazolate framework nanocomposite for efficient photocatalytic CO$_2$ reduction. *ACS Energy Lett.* **2018**, 2656–2662. [CrossRef]

20. Mollick, S.; Mandal, T.N.; Jana, A.; Fajal, S.; Desai, A.V.; Ghosh, S.K. Ultrastable luminescent hybrid bromide perovskite@MOF nanocomposites for the degradation of organic pollutants in water. *ACS Appl. Nano Mater.* **2019**, *2*, 1333–1340. [CrossRef]

21. Wan, S.P.; Ou, M.; Zhong, Q.; Wang, X.M. Perovskite-type CsPbBr$_3$ quantum dots/UiO-66(NH$_2$) nanojunction as efficient visible-light-driven photocatalyst for CO$_2$ reduction. *Chem. Eng. J.* **2019**, *358*, 1287–1295. [CrossRef]

22. Wang, D.K.; Wang, M.T.; Li, Z.H. Fe-Based metal-organic frameworks for highly selective photocatalytic benzene hydroxylation to phenol. *ACS Catal.* **2015**, *5*, 6852–6857. [CrossRef]

23. Liang, R.W.; Luo, S.G.; Jing, F.F.; Shen, L.J.; Qin, N.; Wu, L. A simple strategy for fabrication of Pd@MIL-100(Fe) nanocomposite as a visible-light-driven photocatalyst for the treatment of pharmaceuticals and personal care products (PPCPs). *Appl. Catal. B* **2015**, *176*, 240–248. [CrossRef]

24. Hong, J.D.; Chen, C.P.; Bedoya, F.E.; Kelsall, G.H.; O'Hare, D.; Petit, C. Carbon nitride nanosheet/metal-organic framework nanocomposites with synergistic photocatalytic activities. *Catal. Sci. Technol.* **2016**, *6*, 5042–5051. [CrossRef]

25. Zheng, J.J.; Jiao, Z.B. Modified Bi$_2$WO$_6$ with metal-organic frameworks for enhanced photocatalytic activity under visible light. *J. Colloid Interface Sci.* **2017**, *488*, 234–239. [CrossRef]

26. Zhang, C.F.; Qiu, L.G.; Ke, F.; Zhu, Y.J.; Yuan, Y.P.; Xu, G.S.; Jiang, X. A novel magnetic recyclable photocatalyst based on a core-shell metal-organic framework Fe$_3$O$_4$@MIL-100(Fe) for the decolorization of methylene blue dye. *J. Mater. Chem. A* **2013**, *1*, 14329–14334. [CrossRef]

27. Parvinizadeh, F.; Daneshfar, A. Fabrication of a magnetic metal-organic framework molecularly imprinted polymer for extraction of anti-malaria agent hydroxychloroquine. *New J. Chem.* **2019**, *43*, 8508–8516. [CrossRef]

28. Chaturvedi, G.; Kaur, A.; Umar, A.; Khan, M.A.; Algarni, H.; Kansal, S.K. Removal of fluoroquinolone drug, levofloxacin, from aqueous phase over iron based MOFs, MIL-100(Fe). *J. Solid State Chem.* **2020**, *281*, 121029–121038. [CrossRef]

29. Mahmoodi, N.M.; Abdi, J.; Oveisi, M.; Asli, M.A.; Vossoughi, M. Metal-Organic framework (MIL-100 (Fe)): Synthesis, detailed photocatalytic dye degradation ability in colored textile wastewater and recycling. *Mater. Res. Bull.* **2018**, *100*, 357–366. [CrossRef]

30. Huang, J.; Zhang, X.B.; Song, H.Y.; Chen, C.X.; Han, F.Q.; Wen, C.C. Protonated graphitic carbon nitride coated metal-organic frameworks with enhanced visible-light photocatalytic activity for contaminants degradation. *Appl. Surf. Sci.* **2018**, *441*, 85–98. [CrossRef]

31. Li, Z.J.; Hofman, E.; Li, J.; Davis, A.H.; Tung, C.H.; Wu, L.Z.; Zheng, W.W. Photoelectrochemically active and environmentally stable CsPbBr$_3$/TiO$_2$ core/shell nanocrystals. *Adv. Funct. Mater.* **2018**, *28*, 1704288–1704294. [CrossRef]

32. Pal, P.; Saha, S.; Banik, A.; Sarkar, A.; Biswas, K. All-solid-state mechanochemical synthesis and post-synthetic transformation of inorganic perovskite-type halides. *Chem. Eur. J.* **2018**, *24*, 1811–1815. [CrossRef] [PubMed]

33. He, X.; Nguyen, V.; Jiang, Z.; Wang, D.W.; Zhu, Z.; Wang, W.N. Highly-Oriented one-dimensional MOF-semiconductor nanoarrays for efficient photodegradation of antibiotics. *Catal. Sci. Technol.* **2018**, *8*, 2117–2123. [CrossRef]

34. Araya, T.; Chen, C.C.; Jia, M.K.; Johnson, D.; Li, R.; Huang, Y.P. Selective degradation of organic dyes by a resin modified Fe-based metal-organic framework under visible light irradiation. *Opt. Mater.* **2017**, *64*, 512–523. [CrossRef]

35. Tang, X.S.; Hu, Z.P.; Yuan, W.; Hu, W.; Shao, H.B.; Han, D.J.; Zheng, J.F.; Hao, J.Y.; Zang, Z.G.; Du, J.; et al. Perovskite $CsPb_2Br_5$ microplate laser with enhanced stability and tunable properties. *Adv. Opt. Mater.* **2017**, *5*, 1600788–1600795. [CrossRef]

36. Tang, X.S.; Han, S.; Zu, Z.Q.; Hu, W.; Zhou, D.; Du, J.; Hu, Z.P.; Li, S.Q.; Zang, Z.G. All-Inorganic perovskite $CsPb_2Br_5$ microsheets for photodetector application. *Front. Phys.* **2018**, *5*. [CrossRef]

37. Song, P.J.; Qiao, B.; Song, D.D.; Liang, Z.Q.; Gao, D.; Cao, J.Y.; Shen, Z.H.; Xu, Z.; Zhao, S.L. Colour- and structure-stable $CsPbBr_3$-$CsPb_2Br_5$ compounded quantum dots with tuneable blue and green light emission. *J. Alloys Compd.* **2018**, *767*, 98–105. [CrossRef]

38. Gargiulo, V.; Alfe, M.; Raganati, F.; Lisi, L.; Chirone, R.; Ammendola, P. BTC-Based metal-organic frameworks: Correlation between relevant structural features and CO_2 adsorption performances. *Fuel* **2018**, *222*, 319–326. [CrossRef]

39. Pu, Y.C.; Fan, H.C.; Liu, T.W.; Chen, J.W. Methylamine lead bromide perovskite/protonated graphitic carbon nitride nanocomposites: Interfacial charge carrier dynamics and photocatalysis. *J. Mater. Chem. A* **2017**, *5*, 25438–25449. [CrossRef]

40. Tan, F.C.; Liu, M.; Li, K.Y.; Wang, Y.R.; Wang, J.H.; Guo, X.W.; Zhang, G.L.; Song, C.S. Facile synthesis of size-controlled MIL-100(Fe) with excellent adsorption capacity for methylene blue. *Chem. Eng. J.* **2015**, *281*, 360–367. [CrossRef]

41. Zhan, X.S.; Jin, Z.W.; Zhan, J.R.; Bai, D.L.; Bian, H.; Wang, K.; Sun, J.; Wang, Q.; Liu, S.F. All-Ambient processed binary $CsPbBr_3$-$CsPb_2Br_5$ perovskites with synergistic enhancement for high-efficiency Cs-Pb-Br-based solar cells. *ACS Appl. Mater. Interfaces* **2018**, *10*, 7145–7154. [CrossRef] [PubMed]

42. Wang, D.K.; Song, Y.J.; Cai, J.Y.; Wu, L.; Li, Z.H. Effective photo-reduction to deposit Pt nanoparticles on MIL-100(Fe) for visible-light-induced hydrogen evolution. *New J. Chem.* **2016**, *40*, 9170–9175. [CrossRef]